Quantum Correlations in Three-Beam Symmetric Gaussian States Accessed via Photon-Number-Resolving Detection and Quantum Universal Invariants

Jan Peřina Jr.,^{1,*} Nazarii Sudak,² Artur Barasiński,^{2,†} and Antonín Černoch³

¹ Joint Laboratory of Optics of Palacký University and Institute of Physics of CAS, Faculty of Science, Palacký University, 17. listopadu 12, 771 46 Olomouc, Czech Republic ² Institute of Theoretical Physics, University of Wroclaw, Plac Maxa Borna 9, 50-204 Wrocaw, Poland ³ Joint Laboratory of Optics, Institute of Physics of CAS, 17. listopadu 50a, 779 00 Olomouc, Czech Republic

Quantum correlations of symmetric 3-beam Gaussian states are analyzed using their quantum universal invariants. These invariants, 1-, 2-, and 3-beam purities, are expressed in terms of the beams' intensity moments up to sixth order. The 3-beam symmetric Gaussian states with varying amounts of the noise are experimentally generated using entangled photon pairs from down-conversion, their invariants are determined, and their quantum correlations are quantified. The coexistence of biand tripartite entanglement and genuine tripartite entanglement is observed in these states that resemble the noisy GHZ/W states.

I. INTRODUCTION

The discovery of phase-squeezed light [1], whose observation [2] belongs to the first experiments certifying the existence of nonclassical states of light, triggered fast development of the wide area of quantum optics devoted to the properties of bosonic modes with their infinitely large Hilbert spaces [3]. Today, this area, known as continuous-variable (CV) quantum optics, represents a particularly promising avenue to develop different types of quantum technologies applicable, e.g., in quantum information processing and quantum key distribution (QKD) [4]. Compared to other developing quantum technologies (e.g., based on discrete variables), CV states exhibit resilience against decoherence and provide large Hilbert spaces for information encoding. They also allow for purification [5] and entanglement distillation [6]. Moreover, deterministic generation of large entangled states represents the most remarkable attribute of CV fields. CV quantum optics has also become a viable route for quantum computation where realistic squeezing levels above 10 dB [7] are sufficient to achieve fault tolerance [8]. In addition, squeezed states have been found extraordinarily useful in detection of the gravitational waves [9].

Although homodyne tomography [10] of Gaussian states can be reduced to just 2 orthogonal cuts, the use of a local oscillator requires advanced experimental setups. Nevertheless, at present, there exists an alternative promising for practical applications: photon-number-resolving detectors [11]. The fact that they cannot capture the detected-state phase properties does not have to be a drawback. This especially occurs when complete characterization/identification of a measured state does not require phase information due to its properties. Such states can be recognized when we determine their

quantum universal invariants (QUIs) [12] and these QUIs are uniquely determined using only photocount measurements. Such states then immediately become extraordinarily promising for practical applications in various CV-based metrology and quantum information processing protocols.

Here, we show that symmetric three-beam Gaussian states (STBGSs) belong to this kind of states. We note that these states are also known as 3-mode squeezed thermal states and include, among others, the noisy GHZ/W states [13, 14]. They have already demonstrated their effectiveness in the implementation of several CV protocols [15–17]. According to theory, their full identification is reached when we know their 1-, 2-, and 3-beam purities. The main result of our investigations - the formula that gives the 3-beam purity in terms of intensity moments up to the sixth order, together with the formula for the 2beam purity discovered recently [18], then allows for this identification. Subsequently, different forms of quantum correlations can be characterized and classified, including the genuine 3-beam entanglement quantified by the Gaussian cotangle [19]. Finally, using experimental 3beam Gaussian fields generated effectively with the help of parametric down-conversion [18, 20], practicality of the developed approach is demonstrated.

The success in qualitative simplification of the experimental identification of STBGSs poses a natural question: What are the groups of states whose identification does not require the full quantum state reconstruction and what parameters (QUIs) are necessary for the state identification? This question gains particular significance in multipartite systems, where the structure of quantum correlations is more intricate and complex [21] and thus potentially more attractive for various applications. Moreover, our experimental results for 3-beam fields already provide certain insight into understanding whether and how various types of quantum correlations are distributed over many different systems.

The paper is organized as follows. The structure and parametrization of 3-beam symmetric Gaussian states

^{*} jan.perina.jr@upol.cz

[†] artur.barasinski@uwr.edu.pl

are discussed in Sec. II. Their entanglement (steering) is theoretically analyzed in Sec. III (IV). Experimental characterization of STBGSs using intensity moments of different orders is discussed in Sec. V. Also the experimental 1-, 2-, and 3-beam purities and seralian are given in Sec. V, together with other experimental characteristics including mean photon number, the Fano factor, sub-shot-parameter, and the Kullback-Leibler divergence. The properties of the observed genuine tripartite entanglement are analyzed in Sec. VI, together with those belonging to the observed steering. The properties of the corresponding GHZ/W states are discussed in Sec. VII. Sec. VIII brings conclusions. Estimates and bounds for the quantities characterizing STBGSs are discussed in Appendix A assuming knowledge of the intensity moments up to fourth order. The role of the number of measurement repetitions in the determination of experimental errors is addressed in Appendix B.

II. STRUCTURE OF THREE-BEAM SYMMETRIC GAUSSIAN STATES

We consider a CV 3-beam single-mode symmetric system [22] described in the Hibert space $\mathcal{H} = \bigotimes_{j=1}^{3} \mathcal{H}_{j}$, where \mathcal{H}_{j} stands for the infinite-dimensional Fock space of beam j. Let $\hat{x}_j = (\hat{a}_j + \hat{a}_j^{\dagger})$ and $\hat{p}_j = -i(\hat{a}_j - \hat{a}_j^{\dagger})$ be the quadrature operators with a_j (a_i^{\dagger}) denoting the photon annihilation (creation) operator acting on \mathcal{H}_i . The quadrature operators are then collected in the vector $X = (\hat{x}_1, \hat{p}_1, \hat{x}_2, \hat{p}_2, \hat{x}_3, \hat{p}_3)$ with the canonical commutation relations expressed as $[\hat{X}_j, \hat{X}_k] = 2i\Omega_{jk}$, where $\Omega = \bigoplus_{j=1}^{3} \begin{pmatrix} 0 & 1 \\ -1 & 0 \end{pmatrix}$ is the symplectic form. Then, any Gaussian state with its statistical operator $\hat{\rho}_3$ is fully specified, up to local displacement, by its covariance matrix (CM) σ_3 with the matrix elements given by $[\sigma_3]_{jk} = \frac{1}{2}(\langle \hat{X}_j \hat{X}_k + \hat{X}_k \hat{X}_j \rangle) - \langle \hat{X}_j \rangle \langle \hat{X}_k \rangle$. The CM

For future convenience, let us write the CM σ_3 of a STBGS in terms of two-by-two submatrices as

must fulfill the Robertson-Schrödinger uncertainty rela-

tion $\sigma_3 + i\Omega \ge 0$ [23–25].

$$\sigma_3 = \begin{pmatrix} \alpha & \gamma & \gamma \\ \gamma & \alpha & \gamma \\ \gamma & \gamma & \alpha \end{pmatrix}, \tag{1}$$

where $\alpha = \text{diag}(a, a)$ is the local CM corresponding to the reduced state of one beam and $\gamma = \operatorname{diag}(c_+, c_-)$. We note that Eq. (1) refers to the so-called standard form [26, 27]. In our approach, we rely on an alternative parameterization of σ_3 that uses three out of four state invariants [12]. They admit direct interpretation for generic Gaussian states and include global purity $\mu_3 = \text{Det}(\boldsymbol{\sigma}_3)^{-1/2}$, marginal k-beam purities $\mu_k = \text{Det}(\boldsymbol{\sigma}_k)^{-1/2}$ for k = 1, 2, and two-beam Seralian $\Delta_2 = 2 \mathrm{Det}(\boldsymbol{\alpha}) + 2 \mathrm{Det}(\boldsymbol{\gamma}).$

By selecting μ_1 , μ_2 , and Δ_2 as independent parameters (motivated by Ref. [28]), the following relationship can be introduced

$$a = \frac{1}{\mu_1}, \quad c_{\pm} = \frac{1}{4} \sqrt{\mu_1^2 \left(\Delta_2^2 - \frac{4}{\mu_2^2}\right)} \pm \epsilon,$$

$$\epsilon \equiv \frac{1}{4} \sqrt{\frac{(4\mu_1^2 - \mu_1^4 \Delta_2)^2}{\mu_1^6} - \frac{4\mu_1^2}{\mu_2^2}}.$$
(2)

From Eq. (2) one immediately finds that the necessary conditions for a physical state, $c_+ \in \mathbb{R}$, and the Robertson-Schrödinger uncertainty relation, are simultaneously expressed as

$$\mu_1^2 \le \mu_2 \le \mu_1 \quad \text{and} \quad (3)$$

$$\mathcal{F}(\mu_1, \mu_2) \le \Delta_2 \le \min\left\{\frac{4}{\mu_1^2} - \frac{2}{\mu_2}, 1 + \frac{1}{\mu_2^2}\right\}, \quad (4)$$

$$\mathcal{F}(\mu_1, \mu_2) = \begin{cases}
\frac{2}{\mu_2} \quad \text{for } \mu_1^2 \le \mu_2 \le \frac{4\mu_1^2}{3 + \mu_1^2}, \\
\frac{1}{3}\left(2 + \frac{6}{\mu_1^2} - \omega\right) \quad \text{for } \frac{4\mu_1^2}{3 + \mu_1^2} < \mu_2 \le \mu_1
\end{cases}$$

where $\omega = \sqrt{\frac{(\mu_1^2 + 3)^2}{\mu_1^4} - \frac{12}{\mu_2^2}}$. Importantly, both purities μ_1 and μ_2 are experimentally available [18] using the measured intensity moments that are the normally ordered photon-number moments. They are obtained by the Stirling numbers from the measured photon-number moments [29]. For the Seralian Δ_2 , however, only its upper and lower bounds are derived [12], independently of Eq. (4). Nevertheless, in the analyzed symmetric case, Δ_2 can readily be determined from purity μ_3 , as the above analyzed parameters must satisfy the relation

$$\mu_3^{-2} = \text{Det}(\boldsymbol{\sigma}_3) = \frac{1}{2\mu_1^2 \mu_2^3} \left(6\mu_2 - 3\mu_2^3 \Delta_2^2 + \mu_1^2 \mu_2^3 \Delta_2^3 + \sqrt{\mu_2^2 \Delta_2^2 - 4} \left(3\mu_2^2 \Delta_2 - 2\mu_1^2 - \mu_1^2 \mu_2^2 \Delta_2^2 \right) \right).$$
 (5)

This implies that the purities of 2- and 3-beam systems, along with the single-beam purity, are sufficient to fully identify and thus characterize a STBGS. However, the experimental determination of the 3-beam purity using intensity moments is prone to significant errors. This is so since the determination of μ_3 requires intensity moments up to sixth order [12]. Therefore, following the approach in Ref. [18], it is advisable to parameterize the STBGSs by Eq. (2) and replace the Seralian Δ_2 by its minimum and maximum allowed values. In Ref. [18], this method proved useful for obtaining the negativity of 2-beam fields with higher degrees of entanglement. Moreover, combining Eq. (5) with Eq. (4) we reveal the upper and lower bounds for μ_3 in terms of the marginal purities μ_1 and μ_2 .

Despite their simple form, the 3-beam symmetric states σ_3 exhibit a remarkably rich structure of non-

TABLE I. Conditions for observation of different types of correlations characterizing entanglement and Gaussian steering $A \to BC$ and $BC \to A$ in the system with three beams A, B, and C expressed in terms of purities μ_1 and μ_2 .

Degrees of purity	Correlations
Entanglement $A - BC$	
$\mu_1^2 \le \mu_2 \le \frac{3\mu_1^2 + \sqrt{9 + 62\mu_1^2 - 7\mu_1^4 - 3}}{10 - 2\mu_1^2}$	coexistence region I
$\frac{3\mu_1^2 + \sqrt{9 + 62\mu_1^2 - 7\mu_1^4} - 3}{10 - 2\mu_1^2} < \mu_2 \le \frac{\mu_1}{\sqrt{2 - \mu_1^2}}$	coexistence region II
$\frac{\mu_1}{\sqrt{2-\mu_1^2}} < \mu_2 \le \mu_1$	entangled states
Gaussian steering $A \to BC$	
$\mu_1^2 \le \mu_2 \le \frac{\sqrt{16\mu_1^2 + 9} - 3}{2}$	unsteerable states
$\frac{\sqrt{16\mu_1^2 + 9} - 3}{2} < \mu_2 \le \frac{\sqrt{3}\mu_1}{\sqrt{4 - \mu_1^2}}$	coexistence region
$\frac{\sqrt{3}\mu_1}{\sqrt{4-\mu_1^2}} < \mu_2 \le \mu_1$	steerable states
Gaussian steering $BC \to A$	
$\mu_1^2 \le \mu_2 \le \frac{4\mu_1^2}{3+\mu_1^2}$	unsteerable states
$\frac{4\mu_1^2}{3+\mu_1^2} < \mu_2 \le \frac{\sqrt{2}\mu_1}{\sqrt{3-\mu_1^2}}$	coexistence region
$\frac{\sqrt{2}\mu_1}{\sqrt{3-\mu_1^2}} < \mu_2 \le \mu_1$	steerable states

classical correlations. Whereas their entanglement is addressed in detail in the following Sec. III, their steering properties are deeply analyzed in Sec. IV.

III. ENTANGLEMENT IN SYMMETRIC THREE-BEAM GAUSSIAN STATES

Positivity of a partially transposed CM, $\tilde{\sigma}$, has been established as the necessary and sufficient condition for determining the separability of (1 + N)-beam and bisymmetric (M + N)-beam Gaussian states [26–28]. This so-called positive partial transpose (PPT) criterion provides a clear qualitative characterization of the entanglement present in such states. Specifically, a Gaussian state described by the CM σ is separable if and only if all symplectic eigenvalues \tilde{v}_i of its partially transposed CM $\tilde{\sigma}$ satisfy $\tilde{v}_i \geq 1$. Though the converse does not necessarily hold in a generic case, as bound entangled states may also meet the PPT criterion.

For tripartite Gaussian states, a comprehensive qualitative classification of entanglement was presented in Ref. [21], which distinguishes five classes according to their separability under different bipartitions. Among these, only three are relevant for STBGSs: fully inseparable (class 1), bound entangled (class 4), and fully separable (class 5) states. Based on the single-mode and two-mode purities, μ_1 and μ_2 , the corresponding classification is summarized in Table I. Notably, only class 1 states (though not all) can be uniquely identified using marginal purities. For the remaining cases, two coexistence regions emerge: Region I, containing states from

classes 4 and 5 (depending on the value of Δ_2), and Region II, comprising states from classes 1, 4, and 5. The domain of tripartite entanglement shown in Table I coincides with that of pairwise entanglement [30], reflecting the promiscuous sharing of CV entanglement [19]. However, a notable discrepancy arises in coexistence Region II, where states exhibiting tripartite entanglement without any bipartite entanglement are found (see below).

These results emerge in the following calculations. Without loss of generality, we consider the bipartition of the CM σ_3 in the form A-BC, where A, B, and C denote the field beams. In this case, the symplectic eigenvalues of the partially transposed CM $\tilde{\sigma} = \Lambda \sigma \Lambda$, where $\Lambda = \text{diag}(1, -1, 1, 1, 1, 1)$, are given by

$$\tilde{v}_1^2 = (a - c_-)(a - c_+),
\tilde{v}_{\pm}^2 = \frac{1}{2} \left(2a^2 - 3c_-c_+ + a(c_- + c_+) \pm \theta \right),$$
(6)

where

$$\theta = \sqrt{9a^2c_-^2 + 2ac_-c_+(c_- - 7a) + (9a - 7c_-)(a + c_-)c_+^2}.$$

Utilizing Eq. (2), it becomes apparent that \tilde{v}_1 and \tilde{v}_+ remain greater than or equal to 1 throughout the entire domain delineated by Eqs. (3) and (4). Consequently, the entanglement characterization of σ_3 is solely based on \tilde{v}_- . Through this analysis, we have determined that the state σ_3 satisfies the PPT criterion ($\tilde{v}_- \geq 1$) when

$$\mu_1^2 \le \mu_2 \le \frac{3\mu_1^2 + \sqrt{9 + 62\mu_1^2 - 7\mu_1^4} - 3}{10 - 2\mu_1^2},$$
 (7)

for $0 < \mu_1 \le 1$ and all Δ_2 values specified in Eq. (4). This parameter range is hereafter referred to as Region I. Our analysis indicates, however, that satisfying the PPT criterion within Region I does not necessarily guarantee the separability of the states σ_3 . To illustrate this, let us consider a specific example of σ_3 , namely the noisy GHZ/W state. These states are fully characterized by their 1- and 2-beam purities μ_1 and μ_2 or equivalently by the parameters $a = \mu_1^{-1}$ and $n = \mu_1/\mu_2$ (cf. Ref. [31]). We examine two noisy GHZ/W states within Region I: $\{\mu_1, \mu_2\} = \{0.5, 0.25\} \text{ and } \{\mu_1, \mu_2\} = \{0.8, 0.652352\}.$ According to the classification of Refs.[31, 32], the former corresponds to a separable state (class 5), while the latter represents a bound entangled state (class 4). Thus, Region I contains both classes 4 and 5, with the specific class determined by Δ_2 .

On the other hand, one can find that $\tilde{v}_{-} < 1$, i.e. the CMs σ_{3} describe fully inseparable states (class 1), if

$$\frac{\mu_1}{\sqrt{2-\mu_1^2}} \le \mu_2 \le \mu_1,\tag{8}$$

where $0 < \mu_1 \le 1$ and all Δ_2 values specified in Eq. (4). Between these two regions (see Fig. 1), we find the states that belong to one of three classes: class 1, class 4, or class 5. For example, a separable state in this region is

represented by the noisy GHZ/W state with parameters $\{\mu_1, \mu_2\} = \{0.5, 0.28\}$, while a bound entangled state in this region is exemplified by the noisy GHZ/W state with parameters $\{\mu_1, \mu_2\} = \{0.5, 1/(2\sqrt{3})\}$.

In addition to the state classification outlined above, it is also feasible to determine the lower and upper bounds of the 2-beam and 3-beam logarithmic negativities $E_{N,2}$ and $E_{N,3}$ [33–35]. They are defined in general as $E_N \equiv$ $\ln ||\tilde{\rho}||_1$, where $||\cdot||_1$ denotes the trace norm. For Gaussian states, this measure can be determined in terms of the symplectic spectrum \tilde{v} of the partially transposed CM $\tilde{\sigma}$, $E_{\mathcal{N}} = \max\{0, -\sum_{i:\tilde{v}_i < 1} \ln \tilde{v}_i\}$. In this case, only one eigenvalue can take values smaller than 1, and the logarithmic negativity is defined as $E_{N,3} = \max\{0, -\ln \tilde{v}_-\}$. Moreover, since \tilde{v}_{-} in Eq. (6) is monotonic with respect to Δ_2 , the lower and upper bounds of logarithmic negativity are determined by the extremal values of Δ_2 for the fixed 1- and 2-beam purities μ_1 and μ_2 . Specifically, the bounds are given by $E_{N,3}^{\min} = E_N(\max\{\Delta_2\})$ and $E_{N,3}^{\max} = E_N(\min\{\Delta_2\})$. Given the complexity of the resulting expressions, we do not present them explicitly. Instead, we draw $E_{N,3}^{\min}$ and $E_{N,3}^{\max}$ for the symmetric three-beam Gaussian states as they depend on the 'rotated' marginal purities $(\mu_1 + \mu_2)/2$ and $(\mu_1 - \mu_2)/2$ in Figs. 1(c-f).

Finally, the bounds on the logarithmic negativity can be employed to characterize genuine tripartite entanglement through the residual cotangle [19], defined as

$$T_{\pi} = E_{N,3}^2 - 2E_{N,2}^2,\tag{9}$$

where $E_{N,2} = -\frac{1}{2} \ln \left(a^2 - a|c_m - c_p| - c_m c_p\right)$. Using Eq. (2) and following a series of lengthy but straightforward calculations, one can demonstrate that the residual cotangle T_{π} is a monotonic function of Δ_2 . Consequently, it follows that T_{π} attains its maximum and minimum values at the respective boundary values of Δ_2 .

IV. STEERING IN SYMMETRIC THREE-BEAM GAUSSIAN STATES

Gaussian steering is a stronger form of quantum correlation than entanglement [36], playing a key role in asymmetric quantum information tasks such as one-sided device-independent protocols. Due to its directional nature, it exhibits a rich and structured hierarchy of correlations that depend on state purity and symmetry. A detailed classification of the Gaussian-steering properties of STBGSs, based on their marginal purities, is presented in Table I.

Interestingly, STBGSs show no Gaussian steering between individual beams. To demonstrate this, recall that the measure of Gaussian steerability from M to 1—beam subsystems simplifies to [36]

$$\mathcal{G}^{M\to 1}(\sigma) = \max\left\{0, \ln\frac{\mu_{M+1}}{\mu_1}\right\},\tag{10}$$

where μ_1 denotes the purity of a single beam and μ_{M+1} the purity of the joint (M+1)-beam subsystem. From Eq. (10), it follows that fully symmetric states σ_3 cannot exhibit Gaussian steering of type $1 \to 1$, as the condition $\mu_2 > \mu_1$ violates the constraint given in Eq. (3).

However, Gaussian steering emerges between the two-beam and single-beam subsystems. In the $2 \to 1$ scenario, the ratio of purities is given by

$$\frac{\mu_3}{\mu_1} = \frac{\mu_1^2 \mu_2 (\mu_2 \Delta_2 + \gamma)}{3\mu_2 (-\mu_2 \Delta_2 + \gamma) + \mu_1^2 (4 + \mu_2 \Delta_2 (\mu_2 \Delta_2 - \gamma))}, (11)$$

where $\gamma = \sqrt{\mu_2^2 \Delta_2^2 - 4}$. Equation (11) is monotonic in Δ_2 , so its extrema occur at the boundaries of the allowed Δ_2 domain. Consequently, $\mathcal{G}^{2\to 1}(\sigma_3) > 0$ for

$$\frac{\sqrt{2}\mu_1}{\sqrt{3-\mu_1^2}} \le \mu_2 \le \mu_1,\tag{12}$$

where $0 < \mu_1 < 1$ and for all attainable Δ_2 values. The coexistence region, where steering occurs only for certain Δ_2 , is

$$\frac{4\mu_1^2}{3+\mu_1^2} \le \mu_2 < \frac{\sqrt{2}\mu_1}{\sqrt{3-\mu_1^2}},\tag{13}$$

as illustrated in Fig. 2(a).

In the opposite configuration, $1 \rightarrow 2$, the measure of Gaussian steerability is defined as [36]

$$\mathcal{G}^{1\to 2}(\sigma_3) = \max\left\{0, -\sum_{j:\bar{\nu}_j < 1} \ln \bar{\nu}_j\right\},\qquad(14)$$

where $\bar{\nu}_j$ are the symplectic eigenvalues of the Schur complement M_{σ} to single beam CM [37]. For σ_3 , the relevant symplectic eigenvalue is

$$\bar{\nu}^2 = \frac{3\mu_2(-\mu_2\Delta_2 + \gamma) + \mu_1^2(4 + \mu_2\Delta_2(\mu_2\Delta_2 - \gamma))}{2\mu_2^2},$$
(15)

with γ defined below Eq. (11). Since $\bar{\nu}$ is also monotonic in Δ_2 , one finds $\mathcal{G}^{1\to 2}(\sigma_3) > 0$ for

$$\frac{\sqrt{3}\mu_1}{\sqrt{4-\mu_1^2}} \le \mu_2 \le \mu_1,\tag{16}$$

and all allowed Δ_2 . The coexistence region, where steering occurs only for specific Δ_2 , is

$$\frac{\sqrt{16\mu_1^2 + 9} - 3}{2} \le \mu_2 < \frac{\sqrt{3}\mu_1}{\sqrt{4 - \mu_1^2}},\tag{17}$$

as shown in Fig. 2(b).

Both measures, $\mathcal{G}^{2\to 1}(\sigma_3)$ and $\mathcal{G}^{1\to 2}(\sigma_3)$, are monotonic in Δ_2 and thus reach their bounds for max $\{\Delta_2\}$ and min $\{\Delta_2\}$, respectively. The corresponding lower and upper bounds of $\mathcal{G}^{2\to 1}$ and $\mathcal{G}^{1\to 2}$ are plotted in Figs. 2(c—f) as functions of the rotated marginal purities $(\mu_1 + \mu_2)/2$ and $(\mu_1 - \mu_2)/2$.

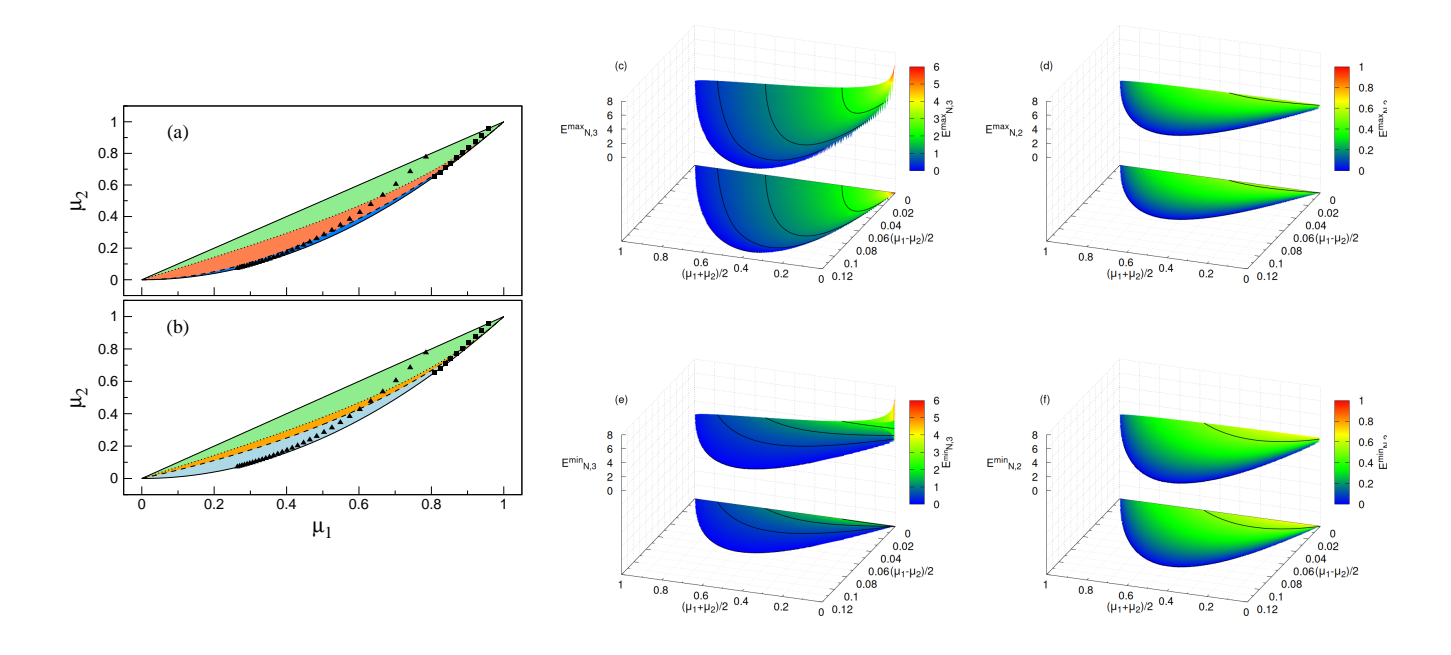


FIG. 1. Two- and three-beam entanglement analyzed in the plane spanned by 1- and 2-beam purities μ_1 and μ_2 . Panel (a) highlights areas differing in 3-beam entanglement properties: Region I (coexistence of separable and bound entangled states) is shown in blue, Region II (coexistence of separable, bound entangled, and fully entangled states) is depicted in orange, the fully entangled region is drawn in green. Panel (b) focuses on 2-beam entanglement: area with 2-beam separable (entangled) states is shown in light blue (green). In the light-orange area separable and entangled states coexist. These regions are classified using the criteria of Ref. [30]. Isolated black boxes (black triangles) refer to the experimental data discussed for M = 6.7 (M = 40) independent modes Upper and lower bounds on three-beam (two-beam) logarithmic negativity $E_{N,3}$ [$E_{N,2}$] are shown in panels (c) [(d)] and (e) [(f)], respectively, as they depend on 'rotated' marginal purities ($\mu_1 + \mu_2$)/2 and ($\mu_1 - \mu_2$)/2. In panels (c) and (e), the black solid curves indicate contour levels of $E_{N,3}$ equal to 0.5, 1, and 2. In panels (d) and (f), the black solid curves correspond to $E_{N,2} = 0.5$.

V. EXPERIMENTAL INVESTIGATION OF QUANTUM CORRELATIONS IN THREE-BEAM SYMMETRIC GAUSSIAN STATES

The above theoretical characterization enables experimentally reliable estimation of CV nonclassical correlations using intensity moments up to fourth order through determination of marginal purities, offering robust sufficient conditions and analytical bounds. Furthermore, since CV logarithmic negativity and Gaussian steering measures are monotonic functions of Δ_2 , the experimental marginal purities also facilitate a reliable estimation of entanglement. This result further enables the estimation of genuine tripartite entanglement via the residual cotangle defined in Eq. (9). Accurate classification of entanglement in the coexistence regions requires the knowledge of Δ_2 , which can be obtained either directly from μ_3 using intensity moments up to sixth order or estimated from the experimental data (see Ref.[12])

Using the experimental photocount technique, a group of STBGSs including those with genuine 3-beam entanglement was prepared and investigated. The state preparation is based on the fact that the Gaussian states are fully characterized just by their first- and second-

order amplitude moments and so they can in principle be constructed from pairwise correlations embedded in twin beams. The underlying principal scheme drawn in Fig. 3 uses three twin beams whose constituting beams contribute differently to beams 1, 2, and 3. Additional beams with increasing intensities then form the noisy parts of STBGSs. Using the technique of compound beams suggested in Ref. [20], all needed beams are derived from a sequence of measurements of photocount distributions of identical weak twin beams by two singlephoton avalanche photodiodes (APDs). The experimental data characterizing the analyzed STBGSs are then obtained by suitable concatenating the data representing the signal and the idler photocounts of these weak twin beams (for details, see Sec. I and Fig. 1 in Supplemental Material (SM) [38]). We note that, when constructing the states, we alternate the signal and the idler beams to arrive at the Gaussian states symmetric in both intensities and correlations. Whereas the correlated parts of all analyzed states are composed of 12 weak twin beams, up-to 180 weak twin beams are used to form the noise parts of the analyzed states.

The experimental data were transformed into photocount histograms $f(c_1, c_2, c_3)$ giving the probability

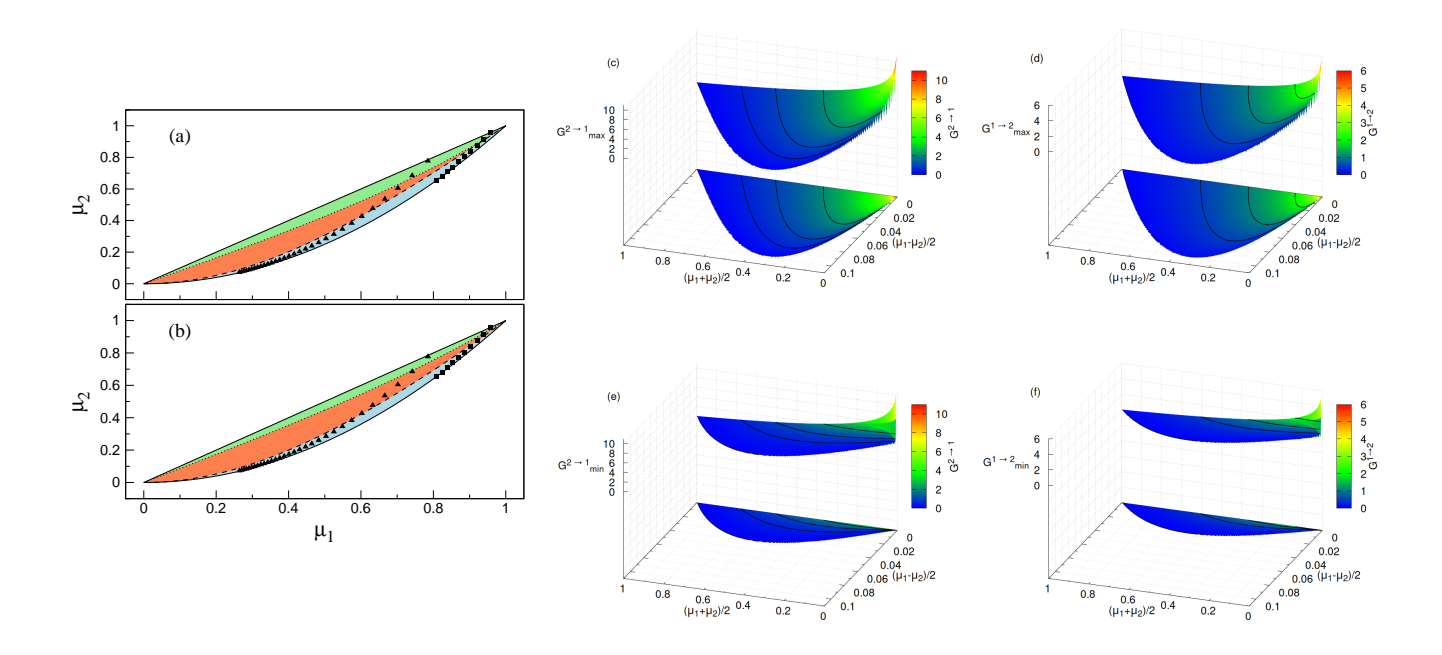


FIG. 2. Three-mode Gaussian steering: Steerable region, coexistence region, and unsteerable region for steering parameters (a) $\mathcal{G}^{2\to 1}$ and (b) $\mathcal{G}^{1\to 2}$ are drawn in turn in green, orange, and blue color in the plane spanned by 1- and 2-beam purities μ_1 and μ_2 . Isolated black boxes (black triangles) refer to the experimental data for M=6.7 (M=40). Upper and lower bounds $\mathcal{G}_{\max}^{2\to 1}$ [$\mathcal{G}_{\max}^{1\to 2}$] and \mathcal{G}_{\min}^{min} [\mathcal{G}_{\min}^{min}] on the steering parameter as they depend on 'rotated' marginal purities ($\mu_1 + \mu_2$)/2 and ($\mu_1 - \mu_2$)/2 are drawn in (c) [(d)] and (e) [(f)], respectively. In (c) – (f), black solid curves correspond to $\mathcal{G}_{\max}^{2\to 1}$, $\mathcal{G}_{\max}^{1\to 2}$, $\mathcal{G}_{\min}^{2\to 1}$, and $\mathcal{G}_{\min}^{1\to 2}$ equal to 0.5, 1, and 2.

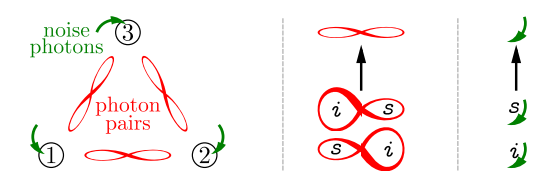


FIG. 3. Structure of 3-beam Gaussian states containing photon-pair (red ∞) and single-photon (green \rightarrow) fields. Both fields can be symmetrized by alternating the signal (s) and the idler (i) beams (double ∞ and \rightarrow)

of measuring simultaneously (c_1, c_2, c_3) photocounts in beams (1, 2, 3). Knowing the parameters of the detectors used, the corresponding photon-number distribution $p(n_1, n_2, n_3)$ was reconstructed using the maximum-likelihood approach [39, 40]. For the model accompanying the experimental results (see Sec. II in SM [38]), parameters of weak twin beams were determined (see Ref. [20]).

The applied technique provided us with 30 compound beams each having around 0.8 mean correlated photons per beam and mean noise photon numbers per beam increasing from 0 to 6. Their main characteristics are quantified using 1-beam mean photon number $\langle n \rangle$ and Fano factor F, 2-beam noise-reduction parameter R, and 2-beam Kullback-Leibler divergence per mode H_2/M . The 1-beam mean photon number $\langle n \rangle$ is plotted in Fig. 4(a)

for the 1-beam mean noise photon number $\langle n_n \rangle$ increasing from 0 to 3. Increasing $\langle n_n \rangle$, the Fano factor F of a beam, $F_1 = 1 + \langle (\Delta W_1)^2 \rangle / \langle W_1 \rangle$, is kept roughly constant [see Fig. 4(b)]. The increase of noise also relatively weakens the pairwise beams correlations contained in the correlated units, which are the source of entanglement of the whole state. Two-beam quantum correlations are quantified in Fig. 4(c) by the noise-reduction parameter R defined as $R_{12} = 1 + \langle [\Delta(W_1 - W_2)]^2 \rangle / (\langle W_1 \rangle + \langle W_2 \rangle)$. For the analyzed states, the noise-reduction parameter R increases from 0.5 to 0.9 because of the noise. The increase of mean noise photon number $\langle n_n \rangle$ also results in lowering inseparability of the 2-beam reduced states [see Fig. 4(d)]. Inseparability of the state is quantified by the two-beam Kullback-Leibler divergence $H_2 \equiv$ $S_{\rm R,1} + S_{\rm R,2} - S_{\rm R,12}$ defined as the difference between the 1-beam and 2-beam Renyi entropies $[S_R = -\ln(\mu)]$. We note that, according to Fig. 4(d), inseparability of the states as determined by the intensity moments up to sixth order is considerably larger than the idealized one derived only from second-order intensity moments (see below).

To discuss quantum correlations, we determine up-to sixth-order intensity moments reduced per mode in each beam (for the reduction, see Sec. III in SM [38]), derive the fields' 1-, 2-, and 3-beam purities μ_1 , μ_2 , and μ_3 , and implement the above theoretical formulas. However, before analyzing the experimental data, we have to address the problem of experimental precision required to

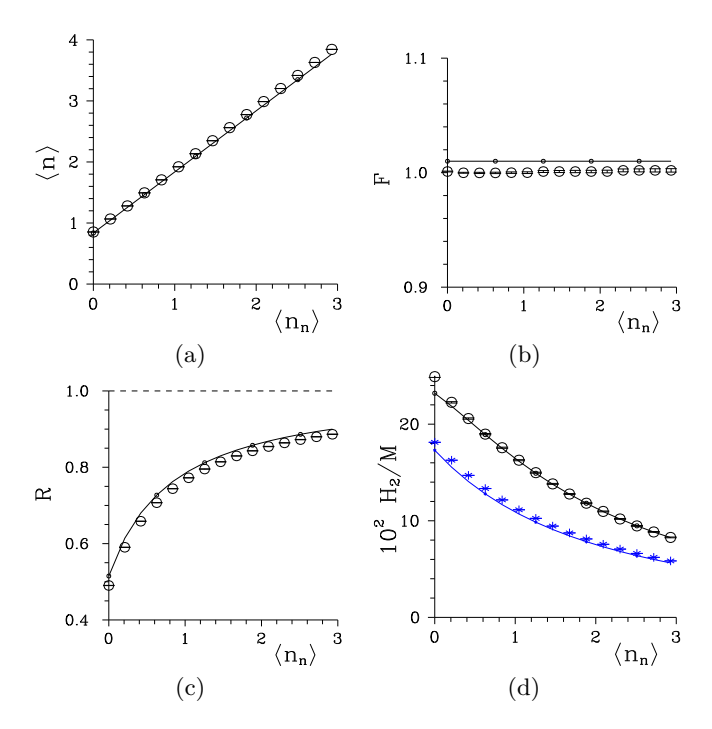


FIG. 4. (a) One-beam mean photon number $\langle n \rangle$, (b) its Fano factor F, (c) 2-beam noise-reduction parameter R, and 2-beam Kullback-Leibler divergence per one typical spatiotemporal mode H_2/M as they depend on 1-beam mean noise photon number $\langle n_{\rm n} \rangle$. Used symbols and curves are described in the caption to Fig. 5. In (b) [(c)], the horizontal dashed line F=1 [R=1] defines the classical-quantum border.

reliably reveal the needed purities. This leads us to three approaches to the data analysis that differ by the number of required measurement realizations.

The usual number of measurement realizations gives the intensity moments up to fourth order with sufficient precision. This gives the purities μ_1 and μ_2 and constraints on possible values of the seralian Δ_2 . The purities μ_1 and μ_2 identify in the single-mode theoretical model a group of compatible STBGSs whose analysis sets the lower (green curves and symbols) and upper (red curves and symbols) bounds for the seralian Δ_2 . Alternatively, we can estimate the value of seralian Δ_2 directly from the experimental intensity moments (see Eq. (5) and Appendix A). Nevertheless, the obtained high-quality data $(6.95 \times 10^8 \text{ measurements on weak twin})$ beams provided $\approx 6.95/6 \times 10^8$ realizations of the analyzed states) allow us to reliably determine the intensity moments up to sixth order. They uniquely identify the state and so give all fields' characteristics (black curves and symbols). On the other hand, having technical applications in mind and assuming the specific form of STBGSs imposed by the used weak twin beams, the second-order intensity moments suffice in the state identification (dark blue curves and symbols, see [41]). Our experimental data suggest that about 10⁸ measurements are needed to completely identify the state (for more details, see Appendix B). About 10⁶ measurements allow us

to safely characterize the state using the lower and upper bounds through fourth-order intensity moments. Finally, only about 10^4 state realizations suffice when we rely only on second-order intensity moments. We note that the analyzed states can directly be emitted in the experiment once the APDs are replaced by photon-number-resolving detectors (see, e.g., in [42]).

We note here that the structure of the experimental fields is richer than that of the single-mode theoretical model and so the above three approaches to the experimental data analysis do not necessarily give compatible predictions for the fields' properties. The more elaborated approach is used, i.e. the higher the intensity moments are involved, the more reliable and more detailed the predictions are. However, the experimental errors must be kept reasonably low.

Considering the intensity moments $\langle w_1^{k_1} w_2^{k_2} w_3^{k_3} \rangle$ reduced per one typical spatio-temporal mode in each beam, the formula for 1-beam purity μ_1 is simple,

$$\mu_1 = \frac{1}{\sqrt{1 + 4\langle w_1 \rangle + 12\langle w_1 \rangle^2 - 4\langle w_1^2 \rangle}}.$$
 (18)

Contrary to this, the formulas for 2- and 3-beam purities μ_2 and μ_3 are rather complex and they can be found in [18] and [12], respectively.

In the analyzed experiment described in detail in Ref. [20], the detectors were characterized by detection efficiencies $\eta_{\rm s}=0.274,~\eta_{\rm i}=0.324$ and dark-count rates $d_{\rm s}=2.8\times 10^{-3},~d_{\rm i}=3.8\times 10^{-3}.$ The application of the above mentioned formulas gave us the purities $\mu_1,~\mu_2,~{\rm and}~\mu_3$ as shown in Fig. 5. They naturally decrease with the increasing mean noise photon number $\langle n_{\rm n} \rangle$. According to the graphs in Figs. 5(a,b,c), we have $\mu_1>\mu_2>\mu_3$ for all experimental STBGSs. Moreover, as the seralian Δ_2 is an important parameter for characterizing the state, we apply Eqs. (4) and (2) to determine its values from those of the purities [see Fig. 5(d)].

The formula (2) also allows us to derive the coefficients a, c_+ , and c_- from the above purities, as shown in Fig. 6. To arrive at the values of coefficients c_+ and c_- , we need to know the 3-beam purity μ_3 , which is experimentally demanding. Alternatively, we may rely only on the experimental values of purities μ_1 and μ_2 and set the lower and upper bounds for the coefficients c_+ and c_- .

VI. OBSERVED QUANTUM CORRELATIONS: GENUINE TRIPARTITE ENTANGLEMENT

The 3-beam correlations in the analyzed states are established by 2-beam correlations (using photon pairs) covering all three beams. This results in the fields' 3-beam entanglement (tripartite entanglement A-BC), quantified by the logarithmic negativity $E_{N,3}$, that naturally decreases with the increasing mean noise photon number $\langle n_{\rm n} \rangle$ [see Fig. 7(a)]. The simplest approach for data processing as well as the most elaborated one suggest that the tripartite entanglement disappears for

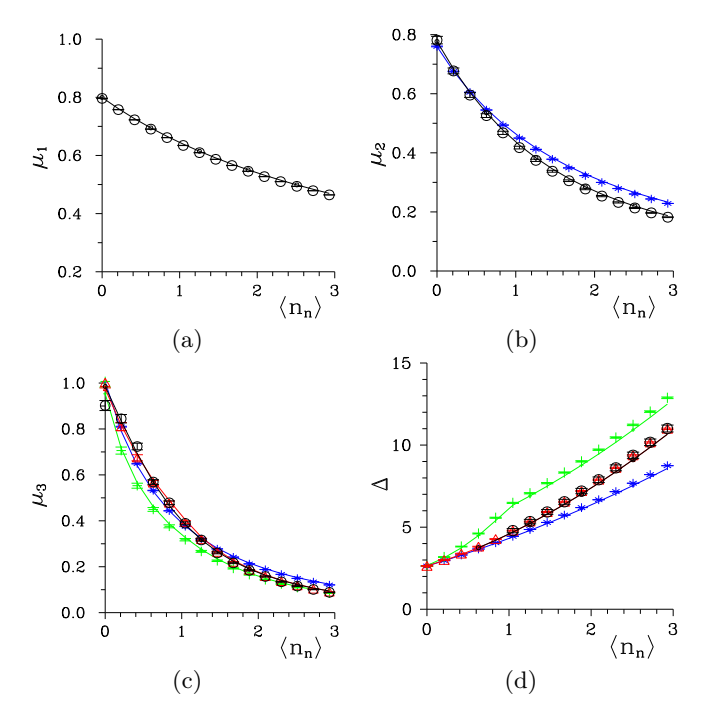


FIG. 5. (a) One-, (b) two-, and (c) 3-beam purities μ_1 , μ_2 , and μ_3 and (d) seralian Δ_2 as they depend on 1-beam mean noise photon number $\langle n_n \rangle$. Isolated symbols with error bars give experimental data, curves originate in the general Gaussian model. Black curves and symbols \circ denote exact values obtained from the intensity moments up to sixth order. The use of moments only up to second order gives blue curves and symbols *. Fourth-order moments provide the lower (green curves and symbols +) and upper (red curves and symbols Δ) estimates for the determined quantities.

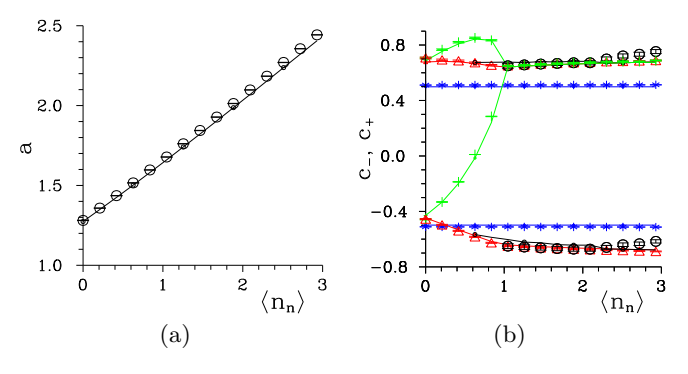


FIG. 6. State coefficients (a) a and (b) c_- and c_+ , $c_- \le c_+$, as they depend on 1-beam mean noise photon number $\langle n_n \rangle$. Symbols and curves are described in the caption to Fig. 5.

 $\langle n_{\rm n} \rangle \approx 2$, i.e. when the noise is approximately 2.5-times larger than the correlated signal. Tripartite entanglement includes contributions from both bipartite entanglement (between beams A-B and A-C) and genuine tripartite entanglement. By quantifying bipartite entanglement using the logarithmic negativity $E_{N,2}$, the genuine tripartite entanglement can be inferred by calculating the residual cotangle [19] introduced in Eq. (9). Following the curves in Fig. 7(b), the bipartite negativ-

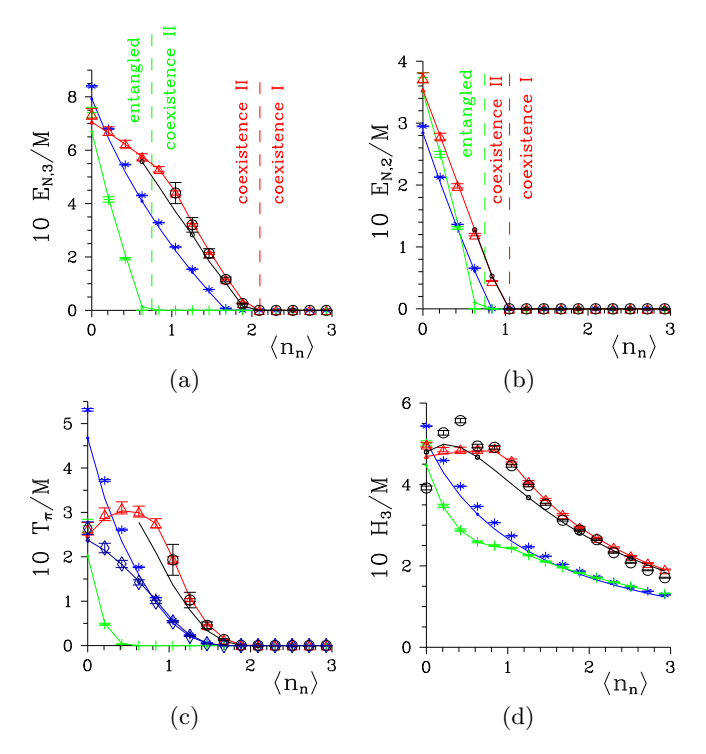


FIG. 7. (a) Tripartite negativity per mode $E_{N,3}/M$, (b) bipartite negativity per mode $E_{N,2}/M$, (c) cotangle per mode T_{π}/M , and (d) 3-beam Kullback-Leibler divergence per mode H_3/M as they depend on 1-beam mean noise photon number $\langle n_{\rm n} \rangle$. Symbols and curves are described in the caption to Fig. 5. In (a) and (b), the point where the green (red) curve nullifies gives the border between entangled (coexistence II) and coexistence II (coexistence I) regions defined in Table I. In (c), navy blue curve and symbols \diamond refer to noisy GHZ/W states identified by μ_1 and μ_2 , as discussed in Sec. VII below.

ity $E_{N,2}$ is lost already for $\langle n_n \rangle$ around 1. As shown in Figs. 7(a,b,c), the fields with $\langle n_{\rm n} \rangle$ below 2 exhibit the genuine tripartite entanglement. In particular, for $\langle n_{\rm n} \rangle$ between 1 and 2, this entanglement persists even in the absence of the bipartite entanglement. Interestingly, inside this region, the values of cotangle T_{π} are significantly lower compared to those observed for $\langle n_{\rm n} \rangle < 1$, which highlights the promiscuous nature of CV entanglement sharing [19]. We note that the properties of the analyzed states are close to those of the noisy GHZ/W states, as evidenced by the corresponding values of cotangle T_{π} in Fig. 7(c) (for details, see Sec. VII below). The approach based on up to fourth-order intensity moments confirms this by determining the upper and lower bounds of these quantities, though it guarantees the genuine tripartite entanglement only for the fields with $\langle n_n \rangle$ smaller than 0.4. We note that, according to Figs. 7(a,b), tripartite entanglement is more resistant against the noise than the bipartite entanglement. Inseparability of 3-beam fields to their one- and two-beam counterparts, quantified by 3-beam Kullback-Leibler divergence $H_3 \equiv S_{R,A} + S_{R,BC} - S_{R,ABC}$ defined in terms of the Rényi-2 entropies $S_{\rm R}$ and plotted in Fig. 7(d), nat-

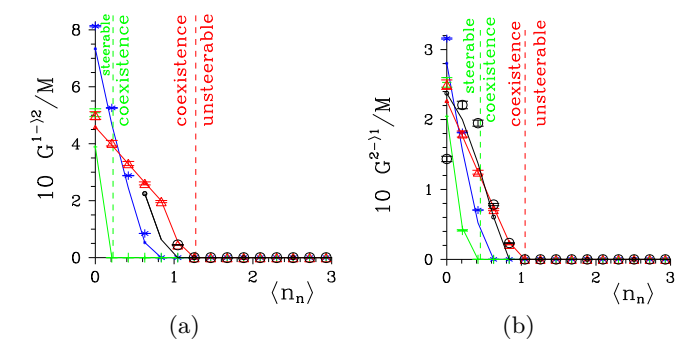


FIG. 8. Three-beam steering parameters per mode (a) $G^{1\to 2}/M$ and (b) $G^{2\to 1}/M$ as they depend on 1-beam mean noise photon number $\langle n_{\rm n} \rangle$. Used symbols and curves are described in the caption to Fig. 5. The point where the green (red) curve nullifies identifies the border between steerable (coexistence) and coexistence (unsteerable) regions defined in Table I.

urally decreases with the increasing $\langle n_n \rangle$.

Steering represents a stronger form of quantum correlations. For our STBGSs, 2-beam steering does not occur. On the other hand, both one beam can steer the remaining two beams (steering parameter $G^{1\to 2}$) and vice versa $(G^{2\to 1})$, as evidenced and quantified in Figs. 8(a,b). Steering by one beam is stronger than its two-beam counterpart, and they are both observed for the states with low amount of the noise $\langle n_n \rangle < 1$.

VII. COMPARISON WITH THEORETICAL NOISY GHZ/W STATES

In the last section, we provide detailed comparison of the properties of the generated states with those of the noisy three-mode GHZ/W states. These states belong to the family of fully symmetric mixed Gaussian states, also known as three-mode squeezed thermal states [32]. The properties of these states were extensively studied in the literature [35]. The noisy GHZ/W states are characterized by two independent parameters, which define a fully symmetric covariance matrix σ_3 that was introduced in Eq. (1). Adopting the parametrization from Ref. [35], the following relations are derived:

$$\mu_3 = \left(\frac{\mu_2}{\mu_1}\right)^3,$$

$$\Delta_2 = \frac{1}{\mu_1^2} + \frac{\mu_1^2}{\mu_2^2}.$$
(19)

The values of purity μ_3 and seralian Δ_2 of the GHZ/W states are compared with those of the generated states in Figs. 9(a) and (b), respectively. Whereas the purities μ_3 of GHZ/W states are close to the upper bound of μ_3 of the generated states from the bottom, the seralians Δ_2 are close to the lower bound of Δ_2 of the generated states from the upper. This means that the GHZ/W states belong the the states with the greatest entanglement among

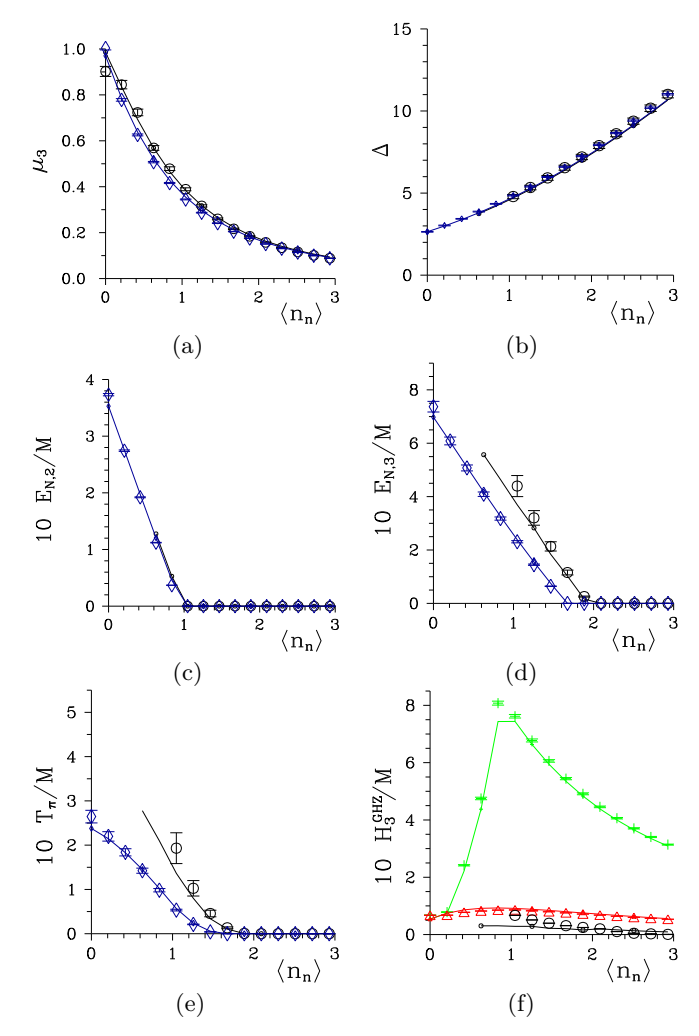


FIG. 9. (a) 3-beam purity μ_3 , (b) seralian Δ_2 , (c) 2-beam negativity per mode $E_{N,2}/M$, (d) 3-beam negativity per mode $E_{N,3}/M$, (e) cotangle per mode T_{π}/M , and (f) 3-beam Kullback-Leibler divergence per mode $H_3^{\rm GHZ}/M$ from the corresponding GHZ/W states as they depend on 1-beam mean noise photon number $\langle n_{\rm n} \rangle$. For GHZ/W states: navy blue curves originate in the general Gaussian model, isolated navy blue symbols \diamond with error bars give experimental data. The remaining symbols and curves are described in the caption to Fig. 5; M=6.7.

the states sharing the purities μ_1 and μ_2 . The corresponding values of 2-beam negativity per mode $E_{N,2}/M$, 3-beam negativity per mode $E_{N,3}/M$, and cotangle per mode T_{π}/M as they vary with the increasing mean noise photon number $\langle n_{\rm n} \rangle$ are plotted by navy blue symbols \diamond and curves in turn in Figs. 9(c), (d), and (e).

The vicinity of the GHZ/W states to the generated states is judged using the Kullback-Leibler divergence $H_3^{\rm GHZ}$ that is determined for the generated states and

the GHZ/W states along the formula:

$$H_3^{\text{GHZ}} = \frac{-3\sqrt{h_1} + h_2}{8\mu_1^4 \mu_2} + \ln\left(\frac{\sqrt{2}\mu_1^4}{\mu_2^2\sqrt{h_3}}\right), \qquad (20)$$

$$h_1 = \left[-4\mu_1^4 + (-4 + \Delta_2\mu_1^2)^2\mu_2^2\right] \left[\mu_1^8 - 10\mu_1^4\mu_2^2 + 9\mu_2^4\right],$$

$$h_2 = 3(-\mu_1^4 + \mu_2^2) \left(8\mu_2 + \mu_1^2\sqrt{-4 + \Delta_2^2\mu_2^2}\right),$$

$$h_3 = 6 + \Delta_2^2(-3 + \Delta_2\mu_1^2)\mu_2^2 - 2\mu_1^2\sqrt{-4 + \Delta_2^2\mu_2^2}/\mu_2 + \Delta_2(3 - \Delta_2\mu_1^2)\mu_2\sqrt{-4 + \Delta_2^2\mu_2^2}$$

$$(21)$$

As evidenced by the values of the Kullback-Leibler divergence per mode $H_3^{\rm GHZ}/M$ plotted in Fig. 9(f) the generated states and the corresponding GHZ/W states are rather close to each other: The greater the mean noise photon number $\langle n_{\rm n} \rangle$ is, the closer the states are.

Similarity of the two kinds of states suggests to apply the entanglement classification developed for the GHZ/W states in [32, 35] to the generated states. The corresponding classification is written as

$$\sqrt{\frac{\mu_1^3}{2-\mu_1}} < \mu_2 \to \mathbf{class} \ \mathbf{1},$$

$$\sqrt{\frac{5\mu_1^4 + 3\sqrt{\mu_1^6(8 + \mu_1^2)}}{18 - 4\mu_1^2}} < \mu_2 \le \sqrt{\frac{\mu_1^3}{2-\mu_1}} \to \mathbf{class} \ \mathbf{4},$$

$$\mu_1^2 < \mu_2 \le \sqrt{\frac{5\mu_1^4 + 3\sqrt{\mu_1^6(8 + \mu_1^2)}}{18 - 4\mu_1^2}} \to \mathbf{class} \ \mathbf{5}. \tag{22}$$

According to this classification the corresponding noisy GHZ/W states fall into class 1 for $\langle n_{\rm n} \rangle < 1.67$ and class 5 for $\langle n_{\rm n} \rangle > 1.88$. Class 4 was not observed, probably owing to the lower number of measurements in the intermediate range of $\langle n_{\rm n} \rangle$.

Furthermore, the coexistence of bi- and tripartite CV entanglement occurs when the conditions $\mu_1 \left(\frac{1+\mu_1^2}{3-\mu_1^2}\right)^{1/2} < \mu_2$ and $\mu_1 < \sqrt{3}\mu_2$ are fulfilled, as discussed in [31]. According to our experimental data, this regime is observed for $\langle n_n \rangle < 1.04$.

VIII. CONCLUSION

Three-beam symmetric Gaussian states were uniquely identified through their universal quantum invariants – 1-, 2-, and 3-beam purities. These invariants were experimentally determined using second-, fourth-, and sixth-order intensity moments obtained through photon-number-resolving detection. The states exhibiting genuine tripartite entanglement and the state featuring the coexistence of two- and three-beam entanglement were observed this way. While the generated states closely resemble the noisy GHZ/W states, our method reveals subtle differences in their properties that demonstrate its sensitivity and reliability. Due to its conceptual simplicity, experimental feasibility, and strong diagnostic power, the presented method has significant potential for broad

applications. It can be readily extended to the study of more complex families of Gaussian states. Foreseen applications span a variety of areas involving multipartite entanglement. This includes characterization of entanglement sources and analysis of quantum states after propagation through various media and communication channels. These insights are particularly relevant for complex multimode optical fields, such as those encountered in quantum networks, quantum communication protocols, and quantum metrology.

ACKNOWLEDGMENTS

J.P. and A.Č. acknowledge support by the project ITI $CZ.02.01.01/00/23_021/0008790$ of the Ministry of Education, Youth, and Sports of the Czech Republic and EU.

Appendix A: Estimates and bounds using fourth-order intensity moments

Fourth-order intensity moments allow for the estimation of the values of seralian Δ_2 in two different ways. In the first one applied in the main text, the 1- and 2-beam purities μ_1 and μ_2 are determined from these moments. Then, using the single-mode theoretical model, all allowed values of the seralian Δ_2 are identified and the lower and upper bounds of Δ_2 are revealed. Then, the upper and lower bounds of 2-beam negativity $E_{N,2}$, 3-beam negativity $E_{N,3}$, and cotangle T_{π} are derived.

In the second, alternative, way the part of seralian Δ_2 expressible directly in terms of intensity moments is computed and the remaining part is estimated via its lower and upper bounds (for details, see [12]). This more straightforward approach limits more the allowed values of $E_{N,2}$, $E_{N,3}$, and T_{π} , as it is apparent from the curves in Figs. 10(b-d,f-h). Comparison of the curves in these figures reveal that whereas the lower bounds from both approaches are close or even identical, the upper bounds from the second approach are considerably more restrictive.

Provided that the experimental fields are divided into M=6.7 independent modes in each beam, the second approach assigns considerably lower values to the cotangle T_{π} than the first approach and identifies the genuine 3-mode entanglement only in the fields with $\langle n_{\rm n} \rangle \leq 1$ [see Fig. 10(d)]. Compared to this, the use of intensity moments up to sixth order reveals 3-beam genuine entanglement in the fields with $\langle n_{\rm n} \rangle \in \langle 1, 2 \rangle$ [see Fig. 7(c)]. However, the use of sixth-order moments is rather demanding for experimental precision and so it fails to identify the genuine 3-beam entanglement for $\langle n_{\rm n} \rangle \leq 1$. This situation demonstrates the importance of simpler approaches in the analysis of experimental data and the need to perform the analysis in consecutive steps starting with the simplest approach and gradually improving

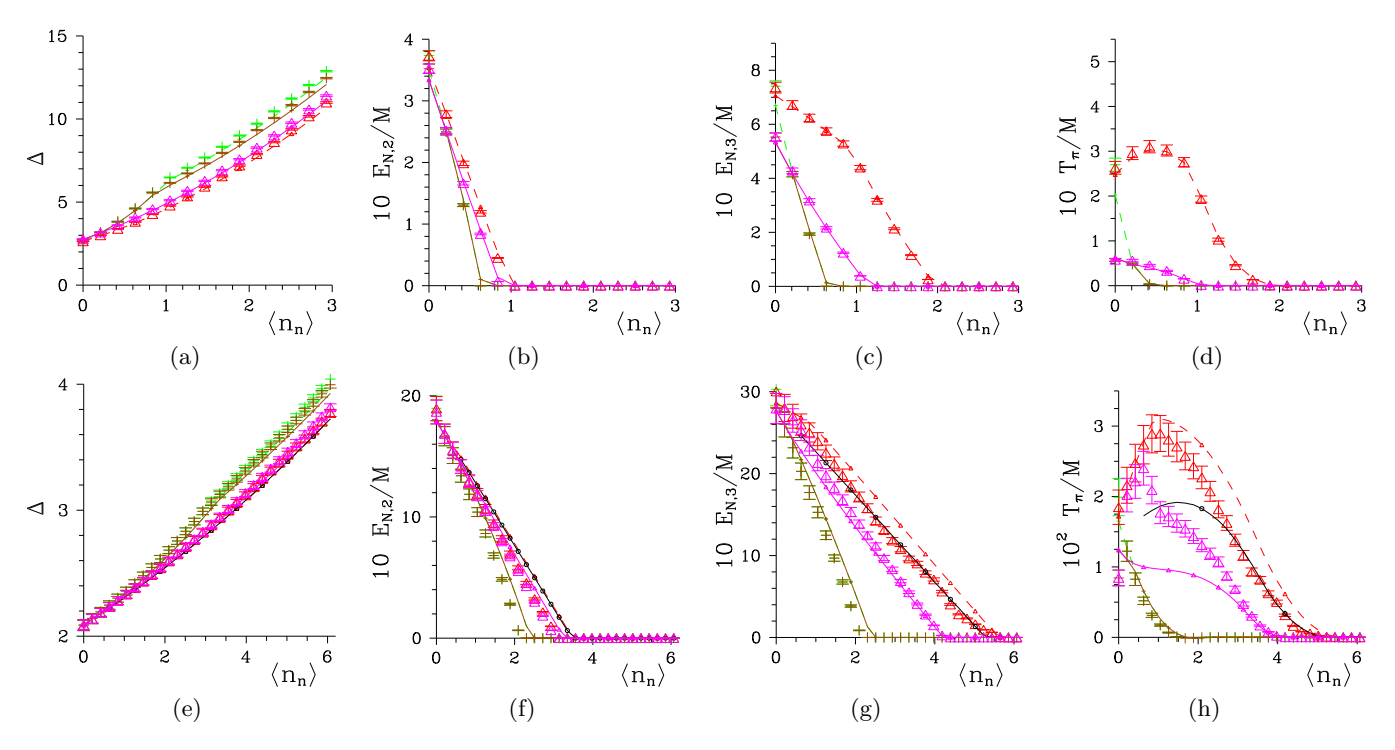


FIG. 10. (a) [(e)] Seralian Δ_2 , (b) [(f)] 2-beam negativity per mode $E_{N,2}/M$, (c) [(g)] 3-beam negativity per mode $E_{N,3}/M$, and (d) [(h)] cotangle per mode T_{π}/M for M=6.7 [M=40] modes as they depend on 1-beam mean noise photon number $\langle n_n \rangle$. Isolated symbols with error bars give experimental data, curves originate in the general Gaussian model. Black curves with \circ in (e—h) denote exact values obtained from the intensity moments up to sixth order. Fourth-order moments provide the lower (green dashed curves and symbols +) and upper (red dashed curves and symbols Δ) bounds for quantum correlations. Direct estimation of the seralian Δ_2 using fourth-order moments results in the lower (brown solid curves and symbols +) and upper (magenta solid curves and symbols Δ) bounds for quantum correlations. Lower bounds for $E_{N,2}/M$, $E_{N,3}/M$, and T_{π}/M are close or even coincide. Symbols and curves for Δ_2 correspond to those for $E_{N,2}/M$, $E_{N,3}/M$, and T_{π}/M .

the knowledge about the investigated states by applying more and more elaborated approaches (that are more and more prone to the experimental errors).

The comparison of results reached by different approaches depends on the number M of independent modes in the beams of the analyzed fields. We note that the beams' division into modes depends on how we use the fields in measurement applications, information processing, etc. Comparing the negativities $E_{N,2}$ and $E_{N,3}$ and cotangle T_{π} in Figs. 10(b-d,f-h) drawn for M=6.7and M = 40, we can see that the greater numbers M of modes make the discrepancies of the results of different approaches considerably smaller. On the other side and considering experimental data, low intensities in singlemode fields (greater number M of modes) mean greater relative errors in determining their intensity moments. These errors prevented us from determining the experimental values of seralian Δ_2 for M=40 in Fig. 10(e) and subsequently the corresponding values of negativities $E_{N,2}$ and $E_{N,3}$ and cotangle T_{π} in Figs. 10(f-h) applying sixth-order intensity moments.

The comparison of curves in Figs. 10(b-d,f-h) demonstrates an important property of quantum correlations – their dependence on the number M of independent modes that constitute the fields. Whereas the genuine 3-beam

entanglement is identified in the fields with $\langle n_{\rm n} \rangle \leq 2$ for M=6.7, it occurs for a much broader group of fields with $\langle n_{\rm n} \rangle \leq 5$ for M=40. This behavior reflects specific influence of the noise when concealing the entanglement of different forms: Dividing an overall field into a greater number of independent modes effectively (partially) prevents entanglement from the detrimental effects of the noise [41].

Appendix B: Experimental errors and the role of the number of measurements

The quantities characterizing the experimental STBGSs were determined in three different ways that use in turn up to sixth-order, fourth-order, and second-order intensity moments. The use of intensity moments of different orders puts different requirements on the statistical precision of their determination derived from the number of measurement realizations. To estimate the needed number of measurement repetitions, we draw in Fig. 11 the cotangle per mode T_{π}/M determined for $1/6 \times 10^8$, $1/6 \times 10^7/6$, and $1/6 \times 10^5$ measurement realizations. Whereas the $6.95/6 \times 10^8$ measurement realizations used when drawing the cotangle per mode T_{π}/M

in Fig. 7(c) allows to reliably obtain the sixth-order intensity moments and thus apply all three approaches in analyzing the data, the reduced numbers of measurement repetitions applied in Figs. 11(a,b) suffice to reveal safely the intensity moments only up to the fourth order. Finally, the $1/6 \times 10^5$ measurement repetitions used when drawing the graph in Fig. 11(c) provide only

second-order intensity moments with sufficiently low experimental error: Nevertheless, additional constraints on the form of the analyzed states compensate for such low number of measurement repetitions and they allow to obtain the cotangle per mode T_{π}/M plotted in Fig. 11(c).

- D. Stoler, Equivalence classes of minimum uncertainty packets, Phys. Rev. D 1, 3217 (1970).
- [2] R. E. Slusher, L. W. Hollberg, B. Yurke, J. C. Mertz, and J. F. Valleys, Observation of squeezed states generated by four-wave mixing in an optical cavity, Phys. Rev. Lett. 55, 2409 (1985).
- [3] V. V. Dodonov, Nonclassical states in quantum optics: A squeezed review of the first 75 years, J. Opt. B: Quantum Semiclass. Opt. 4, R1 (2002).
- [4] F. Laudenbach, C. Pacher, C.-H. F. Fung, A. Poppe, M. Peev, B. Schrenk, M. Hentschel, and P. W. H. Hübel, Continuous-variable quantum key distribution with Gaussian modulation the theory of practical implementations, Adv. Quantum Technol. 1, 1800011 (1918).
- [5] A. Franzen, B. Hage, J. DiGuglielmo, J. Fiurášek, and R. Schnabel, Experimental demonstration of continuous variable purification of squeezed states, Phys. Rev. Lett. 97, 150505 (2006).
- [6] S. Grebien, J. Göttsch, B. Hage, J. Fiurášek, and R. Schnabel, Multistep two-copy distillation of squeezed states via two-photon subtraction, Phys. Rev. Lett. 129, 273604 (1922).
- [7] K. Fukui, A. Tomita, A. Okamoto, and K. Fujii, Highthreshold fault-tolerant quantum computation with analog quantum error correction, Phys. Rev. X 8, 021054 (2018).
- [8] N. C. Menicucci, Fault-tolerant measurement-based quantum computing with continuous-variable cluster states, Phys. Rev. Lett. 112, 120504 (2014).
- [9] R. Schnabel, Squeezed states of light and their applications in laser interferometers, Phys. Rep. **684**, 1 (2017).
- [10] A. I. Lvovsky and M. G. Raymer, Continuous-variable optical quantum-state tomography, Rev. Mod. Phys. 81, 299 (2009).
- [11] L. Mandel and E. Wolf, Optical Coherence and Quantum Optics (Cambridge Univ. Press, Cambridge, 1995).
- [12] N. Sudak, J. Peřina Jr., A. Barasiński, and A. Černoch, Efficient characterization of N-beam Gaussian fields through photon-number measurements: Quantum universal invariants, Phys. Rev. Res. 7, 023278 (2025).
- [13] G. Adesso, A. Serafini, and F. Illuminati, Quantification and scaling of multipartite entanglement in continuous variable systems, Phys. Rev. Lett. 93, 220504 (2004).
- [14] G. Adesso, A. Serafini, and F. Illuminati, Multipartite entanglement in three-mode Gaussian states of continuous-variable systems: Quantification, sharing structure, and decoherence, Phys. Rev. A 73, 032345 (2006).
- [15] S. Pirandola, S. Mancini, D. Vitali, and P. Tombesi, Continuous-variable entanglement and quantum-state teleportation between optical and macroscopic vibrational modes through radiation pressure, Phys. Rev. A 68, 062317 (2003).

- [16] H. Yonezawa, T. Aoki, and A. Furusawa, Demonstration of a quantum teleportation network for continuous variables, Nature 431, 430 (2004).
- [17] A. Ferraro and M. G. A. Paris, Multimode entanglement and telecloning in a noisy environment, Phys. Rev. A 72, 032312 (2005).
- [18] A. Barasiński, J. Peřina, and A. Černoch, Quantification of quantum correlations in two-beam Gaussian states using photon-number measurements, Phys. Rev. Lett. 130, 043603 (2023).
- [19] G. Adesso and F. Illuminati, Continuous variable tangle, monogamy inequality, and entanglement sharing in Gaussian states of continuous variable systems, New Journal of Physics 8, 15 (2006).
- [20] J. Peřina Jr., A. Černoch, and J. Soubusta, Compound twin beams without the need of genuine photon-numberresolving detection, Phys. Rev. Applied 16, 024061 (2021).
- [21] G. Giedke, B. Kraus, M. Lewenstein, and J. I. Cirac, Separability properties of three-mode Gaussian states, Phys. Rev. A 64, 052303 (2001).
- [22] (), in the literature, such tripartite CV Gaussian states are commonly referred to as three-mode Gaussian states. However, to account for the multimode structure of the experimental fields, we adopt the term three-beam symmetric Gaussian states to prevent any potential misunderstanding.
- [23] H. P. Robertson, The uncertainty principle, Phys. Rev. 34, 163 (1929).
- [24] E. Schrödinger, Zum Heisenbergschen Unschärfeprinzip, Ber. Kgl. Akad. Wiss. Berlin 24, 296 (1930).
- [25] A. Serafini, Multimode uncertainty relations and separability of continuous variable states, Phys. Rev. Lett. 96, 110402 (2006).
- [26] R. Simon, Peres-Horodecki separability criterion for continuous variable systems, Phys. Rev. Lett. 84, 2726 (2000).
- [27] L.-M. Duan, G. Giedke, J. I. Cirac, and P. Zoller, Inseparability criterion for continuous variable systems, Phys. Rev. Lett. 84, 2722 (2000).
- [28] A. Serafini, G. Adesso, and F. Illuminati, Unitarily localizable entanglement of Gaussian states, Phys. Rev. A 71, 032349 (2005).
- [29] J. Peřina, Quantum Statistics of Linear and Nonlinear Optical Phenomena (Kluwer, Dordrecht, 1991).
- [30] G. Adesso, A. Serafini, and F. Illuminati, Determination of continuous variable entanglement by purity measurements, Phys. Rev. Lett. 92, 087901 (2004).
- [31] G. Adesso, A. Serafini, and F. Illuminati, Optical state engineering, quantum communication, and robustness of entanglement promiscuity in three-mode Gaussian states, New J. Phys. 9, 60 (2007).

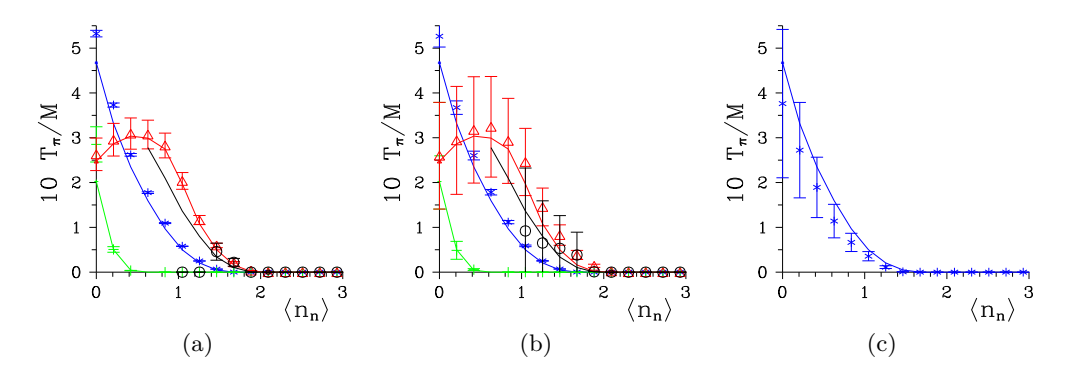


FIG. 11. Cotangle per mode T_{π}/M for M=6.7 modes as they depend on 1-beam mean noise photon number $\langle n_{\rm n} \rangle$ determined from an ensemble containing (a) $1/6 \times 10^8$, (b) $1/6 \times 10^7$, and (c) $1/6 \times 10^5$ measurement realizations. Symbols and curves are described in the caption to Fig. 5.

- [32] X.-Y. Chen, Entanglement bounds of tripartite squeezed thermal states, Phys. Lett. A **335**, 121 (2005).
- [33] S. A. Hill and W. K. Wootters, Computable entanglement, Phys. Rev. Lett. 78, 5022 (1997).
- [34] R. Horodecki, P. Horodecki, M. Horodecki, and K. Horodecki, Quantum entanglement, Rev. Mod. Phys. 81, 865 (2009).
- [35] G. Adesso and F. Illuminati, Entanglement in continuous-variable systems: recent advances and current perspectives, J. Phys. A **40**, 7821 (2007).
- [36] I. Kogias, A. R. Lee, S. Ragy, and G. Adesso, Quantification of Gaussian quantum steering, Phys. Rev. Lett. 114, 060403 (2015).
- [37] (), for STBGSs the Schur complement is given by $M_{\sigma} = \begin{pmatrix} \alpha & \gamma \\ \gamma & \alpha \end{pmatrix} \begin{pmatrix} \gamma \\ \gamma \end{pmatrix} \alpha^{-1} \begin{pmatrix} \gamma & \gamma \end{pmatrix}$.
- [38] See Supplemental Material at for the structure of the analyzed experimental multi-mode fields, experimental

- setup, reconstruction of experimental photocount histograms, multi-mode Gaussian model, and relation between multi-mode and single-mode intensity moments of 3-beam Gaussian fields.
- [39] A. P. Dempster, N. M. Laird, and D. B. Rubin, Maximum likelihood from incomplete data via the EM algorithm, J. Royal Statist. Soc. B **39**, 1 (1977).
- [40] Y. Vardi and D. Lee, From image deblurring to optimal investments: Maximum likelihood solutions for positive linear inverse problems, J. Royal Statist. Soc. B 55, 569 (1993).
- [41] I. I. Arkhipov, J. Peřina Jr., J. Peřina, and A. Miranowicz, Comparative study of nonclassicality, entanglement, and dimensionality of multimode noisy twin beams, Phys. Rev. A 91, 033837 (2015).
- [42] V. Michálek, J. Peřina Jr., and O. Haderka, Experimental quantification of the entanglement of noisy twin beams, Phys. Rev. Applied 14, 024003 (2020).